NANO LETTERS
Letter
Cite This: Nano Lett. 2018, 18, 6995−7003
pubs.acs.org/NanoLett

Ultralarge Modulation of Fluorescence by Neuromodulators in Carbon Nanotubes Functionalized with Self-Assembled Oligonucleotide Rings

Abraham G. Beyene,[†,△] Ali A. Alizadehmojarad,[¶,■,△] Gabriel Dorlhiac,[‡] Natalie Goh,[†] Aaron M. Streets,[‡,§,∥] Petr Král,[#] Lela Vuković,[*,¶] and Markita P. Landry[*,†,∥,⊥]

[†]Department of Chemical and Biomolecular Engineering, [‡]Berkeley Biophysics Program, [§]Department of Bioengineering, and [⊥]California Institute for Quantitative Biosciences (qb3), University of California, Berkeley, Berkeley, California 94720, United States

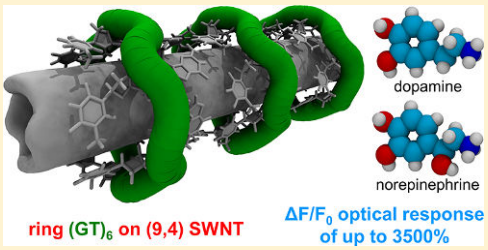
[¶]Department of Chemistry and Biochemistry, University of Texas at El Paso, El Paso, Texas 79968, United States

[∥]Chan-Zuckerberg Biohub, San Francisco, California 94158, United States

[#]Department of Chemistry, Physics, and Biopharmaceutical Sciences, University of Illinois at Chicago, Chicago, Illinois 60607, United States

Supporting Information

ABSTRACT: Noncovalent interactions between single-stranded DNA (ssDNA) oligonucleotides and single wall carbon nanotubes (SWNTs) have provided a unique class of tunable chemistries for a variety of applications. However, mechanistic insight into both the photophysical and intermolecular phenomena underlying their utility is lacking, which results in obligate heuristic approaches for producing ssDNA−SWNT based technologies. In this work, we present an ultrasensitive "turn-on" nanosensor for neuromodulators dopamine and norepinephrine with strong relative change in fluorescence intensity ($\Delta F/F_0$) of up to 3500%, a signal appropriate for *in vivo* neuroimaging, and uncover the photophysical principles and intermolecular interactions that govern the molecular recognition and fluorescence modulation of this nanosensor synthesized from the spontaneous self-assembly of $(GT)_6$ ssDNA rings on SWNTs. The fluorescence modulation of the ssDNA−SWNT conjugate is shown to exhibit remarkable sensitivity to the ssDNA sequence chemistry, length, and surface density, providing a set of parameters with which to tune nanosensor dynamic range, analyte selectivity and strength of fluorescence turn-on. We employ classical and quantum mechanical molecular dynamics simulations to rationalize our experimental findings. Calculations show that $(GT)_6$ ssDNA form ordered rings around (9,4) SWNTs, inducing periodic surface potentials that modulate exciton recombination lifetimes. Further evidence is presented to elucidate how dopamine analyte binding modulates SWNT fluorescence. We discuss the implications of our findings for SWNT-based molecular imaging applications.



KEYWORDS: *Single wall carbon nanotubes, molecular sensing, neuromodulation, molecular dynamics simulations*

Downloaded via UNIV OF ILLINOIS CHICAGO on December 16, 2018 at 00:08:21 (UTC).
See https://pubs.acs.org/sharingguidelines for options on how to legitimately share published articles.

Single wall carbon nanotubes exhibit advantageous electronic and photophysical properties that make them attractive for a diverse field of applications in electronics,[1−5] sensing,[6−9] imaging,[10−13] and molecular transport.[14−16] SWNT fluorescence originates from radiative recombination of one-dimensional confined excitons, exhibits exceptional photostability, and is remarkably sensitive to the nanotube geometric and electronic structure as well as the local chemical environment.[17−19] The sensitivity of SWNT fluorescence to the local chemical environment has been leveraged for the synthesis of optical probes in which polymer functionalizations serve a dual purpose of forming stable SWNT colloidal suspensions and conferring selective molecular recognition capabilities.[9,20] Several SWNT-based probes with selective analyte mediated modulations in optical band gaps or in fluorescence quantum yield with $\Delta F/F_0$ on the order of 9−80% have been reported.[9,21−25]

For *in vivo* molecular sensing applications, synthesizing suitable elements capable of transducing *in vivo* signals constitutes a formidable challenge, requiring maximal changes in fluorescence intensity from baseline ($\Delta F/F_0$) and analyte selectivity appropriate for the biological system under study.[26] The spatiotemporal sensitivity required for *in vivo* utility, in particular for fast processes such as chemical neurotransmission in the brain, must account not only for analyte concentration levels, but also for the spatial spread of the signal (micrometers) as well as its temporal duration (milliseconds).[27,28] Therefore, an ideal probe must satisfy several requirements including high sensitivity, molecular

Received: July 18, 2018
Revised: October 15, 2018
Published: October 17, 2018

© 2018 American Chemical Society

DOI: 10.1021/acs.nanolett.8b02937
Nano Lett. 2018, 18, 6995−7003

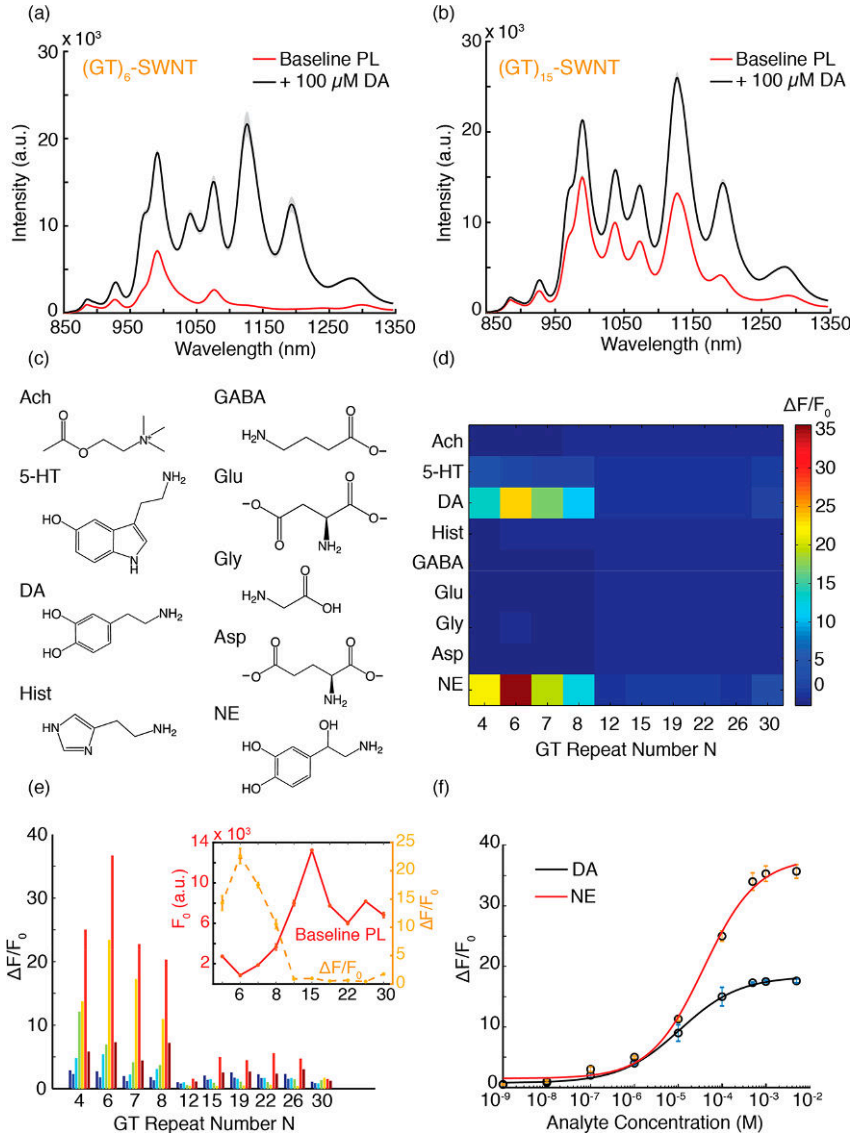


Figure 1. Nanosensor response and selectivity for neuromodulators dopamine and norepinephrine as a function of polymer length. (a, b) Near-infrared fluorescence spectra of $(GT)_6$–SWNT and $(GT)_{15}$–SWNT suspensions before (red trace) and after (black trace) addition of 100 μM dopamine (DA). Mean traces and standard deviation bands from n = 3 measurements are presented. (c, d) Neurotransmitter analyte library chemical structure and heat map of $\Delta F/F_0$ screen against $(GT)_N$–SWNT library. Analyte abbreviations: Ach = acetylcholine, 5-HT = serotonin, DA = dopamine, Hist = histamine, GABA = γ-aminobutyric acid, Glu = glutamate, Gly = glycine, Asp = aspartate, NE = norepinephrine. Heat maps $\Delta F/F_0$ are computed for the peak intensity of the (9,4) SWNT chirality (~1127 nm center wavelength) from the convoluted spectra and all measurements were made at pH ~ 7. (e) $\Delta F/F_0$ of each sequence suspension, for each SWNT chirality: (8,3) dark blue, (6,5) blue, (7,5) cyan, (10,2) green, (9,4) and (7,6) yellow, (8,6) and (12,1) red, and (10,3) and (10,5) maroon. Insert: Baseline fluorescence intensity of $(GT)_N$ suspensions of the (9,4) chirality (red trace) and change in its fluorescence intensity after addition of 100 μM of dopamine (orange trace). (f) $(GT)_6$–SWNT nanosensor response curve for norepinephrine (red) and dopamine (black) computed for the (9,4) SWNT peak intensity. Error bars are standard deviation from n = 3 independent measurements. Experimental data (circles) were fit with Hill equation (solid line).

selectivity, and optimal binding kinetics, among others. The versatility and ease with which SWNTs can be functionalized by a wide range of polymers provides a great opportunity for a rational design of synthetic optical probes capable of detecting biomolecules such as neurotransmitters in their native environment.[8] However, despite proliferating reports of SWNT–polymer conjugates for biomolecule sensing, a robust pathway for translating SWNT nanosensors into *in vivo* sensing applications remains elusive. We identify two specific limitations in the development of SWNT based optical probes, lack of a rational design principle and dearth of *in vivo* implementation, and posit that a lack in fundamental understanding of how SWNT–polymer hybrid nanomaterials interact with and subsequently undergo selective fluorescence modulation by molecular targets underlies these limitations. This knowledge gap is evident in the status quo for nanosensor discovery, which relies on low-throughput screening techniques, and an inability to tune nanosensor performance once a discovery has been made.

In this work, we report a high turn-on nanosensor for neuromodulators dopamine and norepinephrine. We demonstrate that we can tune SWNT baseline fluorescence intensities to increase nanosensor analyte sensitivity and selectivity for key neurotransmitters dopamine and norepinephrine by over

DOI: 10.1021/acs.nanolett.8b02937
Nano Lett. 2018, 18, 6995–7003

an order of magnitude compared to a previously reported catecholamine nanosensor.[21] Sequence-specific "short" ssDNA polymers produced strongly quenched SWNT baseline fluorescence and a robust turn-on response to neuromodulators dopamine and norepinephrine. We find this phenomenon to be sensitive to the base sequence chemistry, polymer contour length, nanotube diameter, and polymer surface density. Classical molecular dynamics (MD) calculations identified polymer-induced 'electrostatic footprinting' on the SWNT surface that induced periodic charge density isosurfaces. The surface potentials modulate SWNT exciton recombination and play a critical role in setting the baseline fluorescence of the ssDNA−SWNT conjugate. Further experimental and quantum mechanical MD (QMMD) simulations suggest a mechanism by which dopamine causes recovery of SWNT fluorescence. Experiments revealed the presence of specific molecular recognition sites in the ssDNA−SWNT corona that stabilize the surface adsorbed polymer when occupied by dopamine and norepinephrine analytes. QMMD simulations show that adsorbed dopamine analytes perturb the periodicity of the ssDNA polymer induced SWNT surface potentials, allowing a competitive radiative relaxation of excitons and a strong nanosensor fluorescence turn-on response.

Strong Fluorescent "Turn-on" Neuromodulator Nanosensors. Prior work has shown that the fluorescence intensity of $(GT)_{15}$−SWNT increases by 60% ($\Delta F/F_0 = 0.6$) upon exposure to 100 μM of dopamine, which translates to $\Delta F/F_0 = 0.3$ at maximal physiological dopamine concentrations that follow burst neuronal firing events (~1 μM).[21,28,29] Here, we denote the baseline (pre-analyte) fluorescence as F_0 and the post-analyte fluorescence as F and define $\Delta F/F_0 = (F - F_0)/F_0$. Motivated by the goal of producing an *in vivo* compatible neuromodulator nanosensor for a broader dynamic range of physiological relevance, we synthesized a $(GT)_N$ based ssDNA−SWNT library for N = 4, 6, 7, 8, 12, 15, 19, 22, 26, and 30 with a previously described protocol.[30] Near infrared fluorescence and absorption spectroscopy confirm that all sequences from N = 4 to N = 30 produced stable DNA−SWNT suspensions, as evidenced by sharply defined spectral line shapes corresponding to known SWNT electronic transitions (Figures 1a,b, S1, and S2). We then measured each $(GT)_N$−SWNT nanosensor response to 100 μM dopamine. Consistent with previous results, dopamine addition increases SWNT fluorescence for all sequences (Figure 1). However, there exists a strong polymer length-dependent trend in nanosensor response, for which the previously reported $(GT)_{15}$−SWNT nanosensor represents an apparent minimum ($\Delta F/F_0 = 0.9$), and $(GT)_6$−SWNT a maximum ($\Delta F/F_0 = 23$) (Figure 1). "Short" $(GT)_N$ polymers (N = 4, 6, 7, 8) yield $\Delta F/F_0$ = 14, 23, 17, and 10 in response to 100 μM dopamine, respectively, for the (9,4) SWNT chirality. Conversely, "long" $(GT)_N$ polymers (N = 12, 15, 19, 22, 26, 30) yield lower $\Delta F/F_0$ = 0.9, 0.9, 0.5, 0.6, 0.4, and 1.8 responses to 100 μM dopamine concentration, respectively (Figure 1b). We identify low baseline fluorescence, F_0, for "short" $(GT)_{4-8}$−SWNT complexes as the reason for the large $\Delta F/F_0$ values of these constructs (Figures 1a,e(insert), S2, and S3). We further note that the (GT) base sequence was found to be uniquely selective for catecholamines over other tested sequences such as $(GA)_6$ (Figure S4); thus, we did not change the polymer base sequence identity for nanosensor optimization and only screened the length-effect of $(GT)_N$ polymers. Interestingly, the $(GT)_6$−SWNT construct also shows increased selectivity toward a new neuromodulator target, norepinephrine, with $\Delta F/F_0 = 35$ sensitivity (Figure 1d,f).

Our experimental results thus identify polymer length as a key modulator of SWNT fluorescence quantum yield, which can be exploited for maximizing nanosensor sensitivity and improving selectivity for neuromodulators. Larger diameter SWNT chiralities exhibited the strongest fluorescence modulation (lowest baseline fluorescence and strongest response to analytes), with the trend emerging most strongly for SWNT with diameters larger than the (6,5) species (Figures 1e, S2, and S3). This apparent diameter dependence will be discussed later. We further identify the $(GT)_6$−SWNT complex as the most suitable nanosensor for imaging both dopamine and norepinephrine, with $\Delta F/F_0$ = 23 and 35, respectively, upon addition of 100 μM analyte concentrations. DNA−SWNT absorption spectra remain largely invariant to the addition of dopamine and norepinephrine (Figure S1), further suggesting that quantum yield increases drive the increase in nanosensor fluorescence. We next validated the utility of $(GT)_6$−SWNT to image dopamine and norepinephrine for *in vivo* relevant concentrations. Concentration-dependent fluorescence response curves for $(GT)_6$−SWNT show fluorescence modulations lie within an optimal dynamic range for *in vivo* imaging of neuromodulation (100 nM to 2 μM) (Figure 1c).[29,31,32] At basal dopaminergic and noradrenergic neuronal activity corresponding to at-rest conditions (50−100 nM), we observe that the $(GT)_6$−SWNT construct exhibited $\Delta F/F_0$ values on the order of 1 (100%).[29,31,32] At burst firing neuronal activity level typically arising from behavioral response to salient events (1−2 μM), $\Delta F/F_0$ values on the order of 5 (500%) can be obtained (Figure 1f).[29,31,32] Equally important, the $(GT)_6$−SWNT construct shows an enhanced selectivity for neuromodulators dopamine and norepinephrine over other potentially competing and ubiquitous neurotransmitters such as glutamate (Glu), acetylcholine (Ach), and γ-aminobutyric acid (GABA) (Figure 1d). We fit our concentration-dependent experimental data points to the Hill equation and determined the dissociation constants (K_d) to be 35 μM for norepinephrine and 10 μM for dopamine (Figure 1f).

The molecular selectivity and sensitivity toward catecholamine neuromodulators appear to be highly dependent on nucleobase chemistry. We found that, among others, two poly-C sequences, C_{30}−SWNT and C_{12}−SWNT, remain largely nonresponsive when exposed to either analyte, consistent with previous studies that show that poly-C ssDNA sequences bind strongly and stably to SWNT (Figure S2).[33] Other 12-mer sequences, including $(GA)_6$, $(ATTT)_3$, and $(TAT)_4$, similarly exhibit no or negligible sensitivity to both dopamine and norepinephrine (Figure S4). The structure of SWNT surface adsorbed ssDNA is sensitive to charge screening by counterions,[34] and recent reports have shown that solution ionic strength plays a role in setting the baseline fluorescence ("brightness") of ssDNA−SWNT constructs.[35] To rule out ionic strength effects, we tested the response of $(GT)_6$−SWNT to both analytes at solution ionic strengths that varied over two orders of magnitude. We found that the turn-on response remained largely insensitive to ionic strength (Figure S4), which suggested that ionic strength may not play a dominant role in determining baseline fluorescence for short $(GT)_N$ sequences. We also tested the $(GT)_6$−SWNT nanosensor response to both analytes at low (pH = 4), neutral (pH = 7),

DOI: 10.1021/acs.nanolett.8b02937
Nano Lett. 2018, 18, 6995−7003

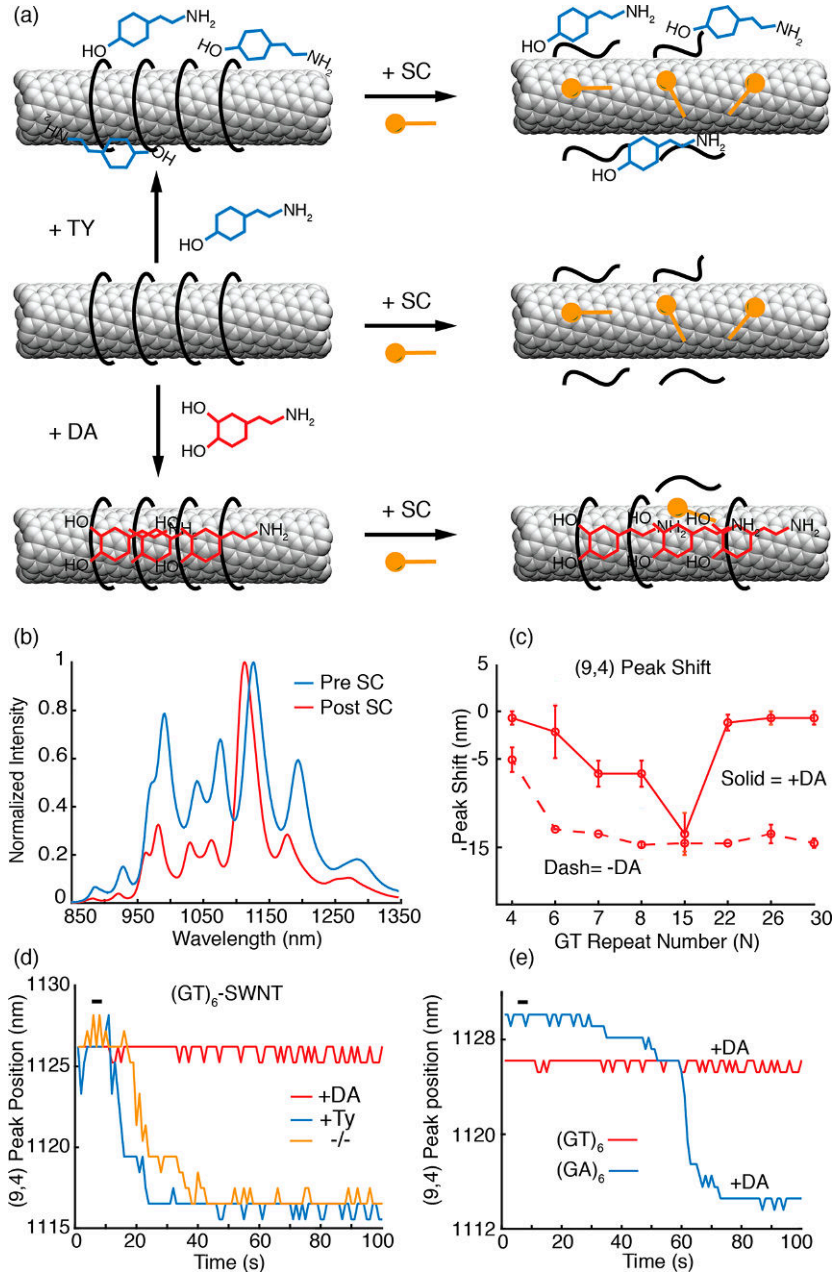


Figure 2. Solvatochromic shifts reveal neuromodulator-specific molecular interactions with nanosensors dependent on ssDNA sequence and length. (a) Middle row: sodium cholate (SC) binds to exposed SWNT surfaces and displaces bound $(GT)_N$ polymers. Bottom row: Nanosensor incubation in dopamine (DA) or norepinephrine (NE) stabilizes ssDNA polymers on the SWNT surface, disallowing SC from accessing the SWNT surface. Top row: Incubation in p-tyramine (TY) does not stabilize surface adsorbed ssDNA against displacement by SC (b) 1 wt % SC induces a solvatochromic shift in SWNT fluorescence. The shift for the $(GT)_6$−SWNT conjugate is presented here as an example. (c) Fluorescence peak shift corresponding to the (9,4) SWNT chirality (~1127 nm) upon exposure to 1 wt % SC without (dash trace) and with (solid trace) preincubation in 10 μM DA. Error bars are standard deviation from n = 3 measurements. Negative peak shits correspond to blue shifting of the peak in the emission spectrum, as shown in panel b. (d) Time-resolved fluorescence measurements of $(GT)_6$−SWNT incubated in 10 μM DA (red trace), 10 μM p-tyramine (TY) (blue trace), and incubated in neither (orange trace). Upon addition of 0.25 wt % SC indicated by the black bar, solvatochromic peak shift in the dopamine incubated corona is eliminated. (e) SC induced solvatochromic peak shift in $(GA)_6$−SWNT incubated in 10 μM of dopamine suggests $(GA)_6$ exhibits short-lived stability on SWNT following dopamine incubation.

and high (pH = 10) conditions. The fluorescence response to dopamine and norepinephrine is observed at all pH conditions, with best responses obtained under physiological pH conditions (Figure S4). We next explored the robustness of the $(GT)_6$−SWNT nanosensor for potential use in measuring endogenous dopamine. Time-dependent fluorescence (Figure S5) and absorbance (Figure S6) measurements (Methods) acquired over the course of 7 days confirm polymer−SWNT stability for all values of N except for N = 4. To probe the stability of our nanosensors in biologically relevant milieus, we tested the ability of $(GT)_6$−SWNT to respond to dopamine in both protein-rich media and in artificial cerebral spinal fluid. We observe robust $\Delta F/F_0$ = 1.43 ± 0.16 turn-on responses to 100 μM dopamine from $(GT)_6$−SWNT nanosensors that were preincubated in cell media (DMEM+ 10% FBS, Methods) (Figure S7a). Furthermore, we tested the compatibility of

DOI: 10.1021/acs.nanolett.8b02937
Nano Lett. 2018, 18, 6995−7003

$(GT)_6$–SWNT nanosensors for use in artificial cerebrospinal fluid (ACSF), a common media used for *ex vivo* brain slice imaging study, and observe nanosensor $\Delta F/F_0$ values of 2.6 ± 0.16 when preincubated in ACSF (Figure S7b). We tested the compatibility of our $(GT)_6$–SWNT nanosensors with potential interfering agents: pharmacological transport inhibitors, and agonists and antagonists of endogenous dopamine receptors. We found that $(GT)_6$–SWNT fluorescence was insensitive to the dopamine transporter inhibitor nomifensine, and dopamine receptor (DRD2) agonist quinpirole, and antagonists sulpiride and haloperidol (Figure S8). $(GT)_6$–SWNT incubated in these drugs retained its strong turn-on response to dopamine (nomifensine, 23.7 ± 1.51; sulpiride, 22.7 ± 0.67; quinpirole, 24.27 ± 0.87; haloperidol, 25.77 ± 0.98; all responses to 100 μM dopamine; mean ± st. dev. from $N = 3$ replicates) permitting the possible use of $(GT)_6$–SWNT constructs in conjunction with drugs that target endogenous receptors and transporters of dopamine. Lastly, single-molecule total internal reflection fluorescence (TIRF) microscopy of surface immobilized $(GT)_6$–SWNT nanosensors (Methods) suggest that ssDNA adsorbed onto SWNT surface is resistant to degradation by endonucleases (Figure S9). We attribute this apparent protective effect to steric hindrance of the SWNT prohibiting substrate access to the nuclease's active site. Lastly, prior work from our lab has shown that molecular recognition using SWNT–polymer conjugates is two-photon compatible, suggesting that several imaging modalities used in neuroimaging can be exploited to image $(GT)_6$–SWNT in biological tissue.[11] Taken together, these results suggest that the $(GT)_6$–SWNT construct can serve as a dopamine and norepinephrine nanosensor with the dynamic range, binding kinetics, and robustness compatible with *in vivo* utility.

Solvatochromic Shifting Reveals Dopamine and Norepinephrine-Specific Molecular Recognition. We performed surfactant displacement experiments to gain further insight into how analytes modulate the quantum yield of $(GT)_N$ polymer functionalized SWNT constructs. Recent work has shown that, when added to DNA–SWNT suspensions, surfactants such as sodium cholate (SC) adsorb to exposed SWNT surface and displace adsorbed ssDNA, thereby altering the SWNT's surface dielectric properties and causing a solvatochromic shift in exciton optical transition energies (Figure 2a,b).[36−38] As expected, addition of SC to $(GT)_N$–SWNT induced solvatochromic shifts in $(GT)_N$–SWNT fluorescence center wavelengths (Figure 2b). All constructs showed characteristic SC-induced blue-shifting of center wavelengths corresponding to SWNT chiralities in the sample. We next repeated SC displacement experiments for all $(GT)_N$–SWNT suspensions preincubated in 10 μM dopamine. Surprisingly, addition of dopamine to $(GT)_N$–SWNT suspensions before addition of SC either reduced or eliminated the SC-induced shifting in exciton optical transitions, suggesting that the surfactant is unable to displace the surface adsorbed ssDNA in the presence of dopamine (Figures 2c and S10a,c,d). We propose that the stabilization of $(GT)_N$ polymers on SWNT arises from a selective interaction between the dopamine analyte and dopamine-specific recognition pockets in the $(GT)_N$–SWNT conjugate and that dopamine trapped in binding pockets enhanced fluorescence by interacting with both the adsorbed polymer and the SWNT. We posit that as a result of these interactions, polymer-mediated binding of analytes selectively enhances the fluorescence quantum yield of ssDNA–SWNT nanosensors, as we further explore using experimental and computational approaches below.

To probe the selectivity of dopamine-induced nanosensor stabilization, we conducted time-resolved SC shift experiments with the $(GT)_6$–SWNT construct in which *p*-tyramine was added to the suspension before addition of SC. Tyramine, a molecular analogue of dopamine differing by one hydroxyl group, does not modulate the fluorescence of $(GT)_6$–SWNT (Figure S11a). We reasoned that the recognition of dopamine and norepinephrine is mediated by unique recognition sites in the $(GT)_6$–SWNT corona and that tyramine's inability to modulate SWNT fluorescence is a consequence of its inability to bind these recognition sites. With this hypothesis, the efficacy of SC in displacing surface adsorbed $(GT)_6$ ssDNA and resulting solvatochromic shift should be unaffected by tyramine. Our results do indeed show that 10 μM tyramine, unlike dopamine, does not attenuate the SC induced peak shifts (Figure 2d), which suggests that tyramine is unable to bind to and stabilize surface adsorbed ssDNA strands.

Our results further indicate that the stability imparted to the SWNT-ssDNA corona phase by the binding of dopamine and norepinephrine is related to the analyte-induced fluorescence modulation specific to the GT base sequence. A $(GA)_6$–SWNT construct, in contrast to $(GT)_6$–SWNT, exhibits negligible modulation in fluorescence upon addition of either dopamine or norepinephrine (Figure S4). We incubated the $(GA)_6$–SWNT suspension in dopamine to measure SC induced peak shifts. We observed that dopamine tentatively stabilized $(GA)_6$–SWNT corona (Figure 2e). However, the dopamine-induced stability of $(GA)_6$–SWNT is short-lived, with distinctive solvatochromic peak shifting occurring with a 60 s delay following SC addition. Another 12-mer sequence, C_{12}, similarly exhibited SC-induced solvatochromic shifting despite the presence of dopamine (Figure S10b). These results suggest that SC-induced peak shifting is a function of both the dopamine-bound fraction of recognition sites in the SWNT–polymer corona and the intrinsic binding affinity between the polymer sequence and SWNT surface.[37] Furthermore, we found that both dopamine and norepinephrine modulate the Raman G^- band of the $(GT)_6$–SWNT between 1500 and 1550 cm^{-1}, whereas *p*-tyramine does not (Figure S12). The increased intensity of the Raman G^- band by dopamine and norepinephrine, but not tyramine, is maintained regardless of the subsequent addition of SC. Absorbance measurements show that addition of analytes does not change the E_{22} transition energies of SWNTs (Figures S1 and S11b) and therefore cannot explain the observed phenomena. A number of interactions can cause changes in Raman intensity or frequency including changes in polymer conformation, solvation dynamics, and variations in local electric field. The presence of degenerate modes in the G^- band of SWNTs further raises the possibility of analyte-mediated symmetry breaking. The persistence of these changes even after SC addition further supports the hypothesis we propose regarding polymer–SWNT–analyte interaction.

We probed whether the surface density of the $(GT)_N$ polymer on the SWNT surface can tune the density of molecular recognitions sites available to analyte. We varied polymer surface packing of the $(GT)_6$–SWNT construct by synthesizing nanosensors with different mass proportions of SWNT (mS) to $(GT)_6$ DNA polymers (mD). The resulting $(GT)_6$–SWNT conjugates thus have variable surface-adsorbed polymer density (Figure S8, Methods) with nominal mS/mD

DOI: 10.1021/acs.nanolett.8b02937
Nano Lett. 2018, 18, 6995−7003

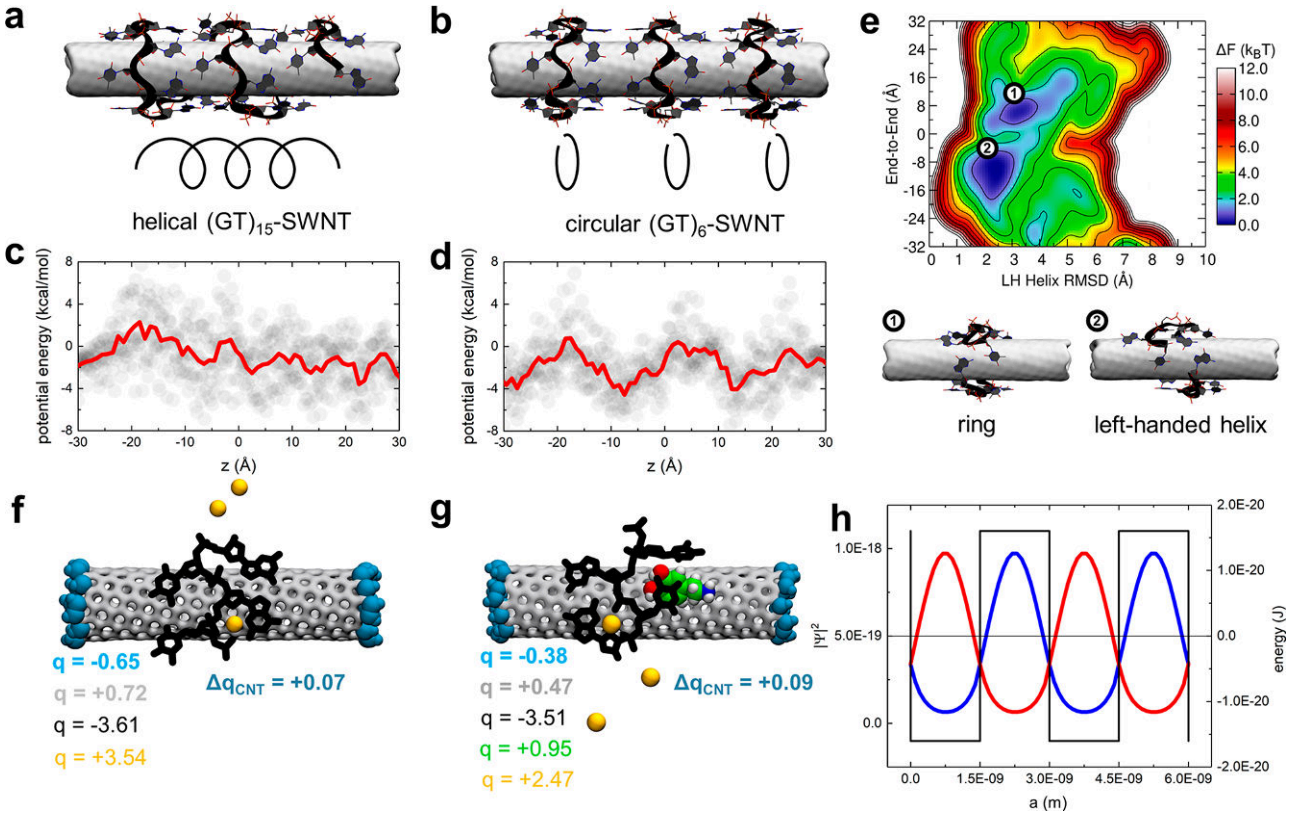


Figure 3. Computational modeling of ssDNA–SWNT nanosensor complexes. (a) Representative conformation of $(GT)_{15}$–SWNT. SWNT is depicted as a gray surface, $(GT)_{15}$ and its backbone are shown in licorice and black ribbon representations, and ssDNA atoms are shown in gray (C), red (O), blue (N), and orange (P). (b) Representative conformation of $(GT)_6$–SWNT, containing three $(GT)_6$ polymers. The color scheme is the same as in panel a. (c) Electrostatic potential energy profile at the SWNT surface in the $(GT)_{15}$–SWNT system as a function of SWNT axial length. The profile is averaged over 2 ns and over the radial SWNT dimension and includes the effects of the complete SWNT environment present in MD simulations (ssDNA, water, and ions). (d) Electrostatic potential energy profile at the SWNT surface for the $(GT)_6$–SWNT system plotted as a function of SWNT axial length. (e) Free energy landscape of $(GT)_6$–SWNT at 300 K. The structures corresponding to two free energy minima are labeled by indices 1 and 2. (f) Net charges of molecular fragments in the $(GT)_2$–SWNT system, evaluated in quantum mechanical calculations. (g) Net charges of molecular fragments in the $(GT)_2$–SWNT system with an adsorbed dopamine molecule, evaluated in quantum mechanical calculations. The color scheme in panels f and g: black (DNA), silver (nonterminal SWNT atoms), blue surface (terminal –CH groups capping the SWNT), yellow (sodium ions), green, blue, red and white spheres (C, N, O, and H atoms on dopamine). (h) Electron (red) and hole (blue) probability densities in a Kronig–Penney potential (Methods). Probability density values are labeled on the left axis, and the values associated with the potential energy well are labeled on the right axis.

mass ratios of 2, 5, and 10, representing a spectrum from "high" to "low" $(GT)_6$ polymer surface density. The resulting fluorescence intensity from equimolar SWNT aliquots shows a clear trend whereby the highest polymer surface densities (mS/mD = 2) exhibit the lowest baseline fluorescence (Figure S8). Addition of 10 μM of dopamine enhances the SWNT fluorescence of all three samples; however, the $\Delta F/F_0$ nanosensor response is highest for the SWNT sample with the highest surface coverage (Figure S13). These results reveal that (i) the degree of baseline fluorescence quenching of SWNT by adsorbed $(GT)_6$ is directly proportional to the polymer surface density; (ii) the higher the polymer surface coverage, the higher the number of dopamine binding pockets; and (iii) dopamine enhances SWNT quantum yield in proportion to the density of bound recognition sites.

Multiscale Simulations of $(GT)_N$ Adsorbed on (9,4) SWNT. We performed multiscale simulations of $(GT)_{(N=6,15)}$–(9,4) SWNT complexes to disclose mechanisms responsible for a strongly quenched baseline fluorescence and a large nanosensor response to neuromodulators observed in $(GT)_6$–SWNT constructs, in contrast to $(GT)_{15}$–SWNT. First, we equilibrated both $(GT)_6$–SWNT and $(GT)_{15}$–SWNT systems with atomistic molecular dynamics (MD) simulations. The $(GT)_{15}$ polymer, which was initially helically wrapped around the SWNT, consistent with previous work,[39−43] remained in a helical conformation during a 200 ns MD simulation (Figure 3a). On the contrary, the $(GT)_6$ polymer on the (9,4) SWNT rearranged from its initial helical conformation into a ring-like conformation in each of the five independent 200 ns trajectories performed, regardless of the handedness of the SWNT simulated (Figures 3b, S22b, and S23). The insensitivity to SWNT handedness is in agreement with previous studies that show that recognition of chiral nanotubes by aromatic systems (graphene ribbons) can only be achieved at low temperatures (200 K) due to small energy differences of different adsorbed states.[44]

We further examined the adsorption of multiple, instead of singular, $(GT)_6$ polymers on the (9,4) SWNT in a 250 ns long simulation. We observed helix-to-ring transitions in all $(GT)_6$ polymers (Figures 3b and S21b). The ring conformations of neighboring $(GT)_6$ ssDNAs become highly ordered throughout the simulation time course, as observed from the distinct sharp peaks positioned at approximately equal intervals of ~0.25 nm in the radial distribution function of DNA

DOI: 10.1021/acs.nanolett.8b02937
Nano Lett. 2018, 18, 6995−7003

phosphate groups (Figure S14). In contrast, $(GT)_6$ polymers adsorbed on the smaller diameter (6,5) SWNT predominantly adopt a helical conformation in a 160 ns long simulation (Figure S22a). Previous simulations of $(GT)_6$ polymers on (8,6) SWNT show that these polymers assume helical and elongated conformations along the SWNT axis, in partial agreement with our results in Figure 3e.[45] However, the ring $(GT)_6$ motif is unique to this study. Differences between these studies may arise from differences in initialization, sampling times, the temperature range selected for the simulated systems, and the complexity of the system.[45]

To confirm that the ring-like conformation is a favorable adsorbed state of $(GT)_6$ on the (9,4) SWNT, we calculated the free energy landscape of this ssDNA on the (9,4) SWNT surface at room temperature (T = 300 K) (Figure 3e) using replica exchange molecular dynamics (Methods).[42] The landscape reveals two distinct stable conformations for $(GT)_6$, a left-handed helix and a nonhelical ring-like conformation, corresponding to free energy minima at (x, y) = (2.5 Å, −10 Å) and (3.2 Å, 6 Å), respectively, where x represents the root−mean−square deviations (RMSD) of the DNA structure with respect to the representative left-handed DNA helix, and y represents the distance along the long SWNT axis of two selected atoms of the 3′- and 5′-end DNA nucleotides. These two conformations have approximately the same free energies, and as such they should both be equivalently present. Moreover, because the free energy barrier between each conformation is only ∼1.2 kcal/mol, frequent interconversions between the two conformations are likely at room temperature for single or sparsely adsorbed polymers. However, in experimental suspensions, SWNT surface is likely to be covered by multiple ssDNA polymers. In that case, the ring-like ssDNA conformations are likely to be prevalent over the helical conformation due to steric hindrance, as the ring-like polymer packing structure provides better ssDNA surface packing on the SWNT. We suggest that the ring-like ssDNA conformation is likely enhanced by the fact that the $(GT)_6$ contour length matches the circumference of the (9,4) SWNT, affording ordered self-assembly of the oligonucleotides on the SWNT surface. On the other hand, the polymer length−SWNT circumference mismatch between $(GT)_6$ and the (6,5) SWNT species renders the ring configuration less likely and favors a helical conformation (Figure S22a). The free energy landscape in Figure 3e also reveals the existence of several local minima, whose associated structures are shown in Figure S24. However, these local minima have higher free energies than the two structures shown in Figure 3e and are likely to be assumed less frequently by the $(GT)_6$ polymer.

Since the charged $(GT)_6$ and $(GT)_{15}$ polymers have different conformations on the (9,4) SWNT, we reasoned that they should create electrostatic potentials of different profiles close to the SWNT surface. To investigate this phenomenon, we calculated the average electrostatic potential at the SWNT surface generated by all molecules in the system (ssDNA, water, and ions, including the Na^+ cations adsorbed over long time scales within ssDNA pockets) (Figures S15 and S16). $(GT)_{15}$ creates regions of negative and positive electrostatic potential under the polymer as a "footprint", which extends ∼4 nm in contiguous length and roughly follow the ssDNA helical pattern (Figure S17a,b). Negative potential pockets are primarily beneath guanine nucleotides, while positive pockets occur beneath thymine nucleotides. When averaged over the radial SWNT dimension, as shown in Figure 3c, the electrostatic potential profile at the SWNT surface under $(GT)_{15}$ is roughly constant across the entire helix, with random fluctuations. The electrostatic potential around SWNT with adsorbed $(GT)_6$ rings also follows the polymer, which results in distinct ring-like regions of alternating positive and negative potentials along the SWNT axis, where each contiguous electrostatic pocket is ∼1.5 nm in length (Figure S17c,d). In contrast to $(GT)_{15}$−SWNT, when averaged over the radial SWNT dimension, these electrostatic potentials exhibit large periodic oscillations across multiple rings (Figure 3d). Therefore, from the perspective of exciton confinement in the SWNT quasi-1D structure, the periodic electrostatic potentials created by the $(GT)_6$ rings effectively form a superlattice (Figure 3d).

Next, QMMD calculations were performed to better understand exciton relaxation in the $(GT)_6$−(9,4) SWNT conjugates (Figure S18). The SWNT is polarized by the presence of the charged DNA polymer, with overall partial positive charges on the SWNT surface covered with ssDNA, and partial negative charges at the SWNT ends (Figure 3f). This charge distribution can be seen as an effective doping of the SWNT, affecting the exciton relaxation processes. In QMMD calculations, we observed a relatively small charge transfer between ssDNA and SWNT (Figure 3f, Table S1). Dopamine adsorption on the DNA-wrapped SWNT slightly decreased the SWNT polarization (Figure 3g and Table S2). However, this effect is only local, and if the molarity of adsorbed dopamine molecules is low, it is unlikely to effectively alter the polarizability of a large $(GT)_6$−SWNT complex (Figures S19 and S20). Conversely, adsorption of dopamine molecules is capable of locally perturbing the periodic electrostatic potential, which can have an effect on SWNT photoluminescence, as we discussed below.

These MD and QMMD results provide insight into possible relaxation pathways of excitons in the $(GT)_N$−SWNT complexes with and without adsorbed dopamine analyte molecules. We thus propose the following mechanisms to explain the strong turn-on response of $(GT)_6$−SWNT nanosensors to dopamine: (i) SWNT polarization induced by the adsorption of multiple $(GT)_6$ polymers can give rise to nonradiative exciton relaxation mechanisms because effective doping activates phonon-assisted relaxation channels for SWNT excitons.[46,47] (ii) At the same time, radiative exciton relaxation in a $(GT)_6$−(9,4)-SWNT complex is expected to be significantly suppressed by the presence of closely spaced periodic potentials of multiple $(GT)_6$ strands (Figure 3d). In positive and negative regions of this potential, the electron and hole wave function components tend to avoid each other (Figure 3h), which results in a significant cancelation of their overlap integral present in the oscillator strength.[48] (iii) However, in the presence of adsorbed dopamine molecules, the cancellation of the overlap integral can be disturbed because of a dopamine-induced disordered superlattice (Figure S21a). Therefore, radiative transitions can become active simultaneously with the nonradiative transitions, giving rise to a fluorescent turn-on nanosensor. Adsorbed dopamine molecules may result in marginal reduction in SWNT polarization and reduce the effective doping caused by the adsorbed $(GT)_6$ rings. However, our work suggests that this mechanism is unlikely to contribute significantly to the turn-on response. We further attribute the SWNT-diameter dependence of the strong turn-on response (Figure 1e, Figure S2) to two phenomena: (i) doping-induced quenching of SWNT

DOI: 10.1021/acs.nanolett.8b02937
Nano Lett. 2018, 18, 6995−7003

photoluminescence becomes more efficient with increasing SWNT diameter[46,47] and (ii) the ordered periodic superlattice formed by $(GT)_{4-8}$ is less likely to occur on smaller diameter SWNTs (Figure S22).

In conclusion, we report $(GT)_6$−SWNT as a strong turn-on optical reporter for the neuromodulators dopamine and norepinephrine, with a dynamical range compatible with applications for *in vivo* neurophysiology. We investigated the photophysical and molecular underpinnings of the strong and selective turn-on response experimentally and computationally. We find that SWNT-ssDNA nanosensors with selective fluorescence modulation toward an analyte exhibit selectivity through specific binding interactions involving the SWNT, the adsorbed polymer, and the analyte. Moreover, the magnitude of a nanosensor turn-on response can be tuned by varying polymer contour length and adsorption surface density. Multiscale computational approaches were used to rationalize our experimental findings. Molecular dynamics simulations revealed that the self-assembly of $(GT)_6$ ssDNA on the SWNT surface produces highly ordered ring structures, which effectively dope the SWNT by polarization and forms a superlattice from the perspective of a 1-D confined SWNT exciton. The effective doping activates exciton nonradiative transitions, while the periodic potential suppresses their radiative relaxation. The baseline SWNT fluorescence, dimmed in this manner, can be selectively enhanced by an analyte that binds selectively to the SWNT surface-adsorbed polymer via perturbation of the superlattice that promotes a competitive radiative relaxation. These insights and results have important implications for the development of nanosensors for specific biomolecular analytes of interest, for tuning the dynamic range of those already developed, and for orthogonal fields of research such as SWNT purification by chiral index and photovoltaics.

■ ASSOCIATED CONTENT

Supporting Information

The Supporting Information is available free of charge on the ACS Publications website at DOI: 10.1021/acs.nanolett.8b02937.

Materials, detailed methods, supplementary figures (PDF)

■ AUTHOR INFORMATION

Corresponding Authors

*E-mail: lvukovic@utep.edu.
*E-mail: landry@berkeley.edu.

ORCID

Petr Král: 0000-0003-2992-9027
Lela Vuković: 0000-0002-9053-5708
Markita P. Landry: 0000-0002-5832-8522

Present Address

■Department of Chemistry, Rice University, Houston, Texas 77005, United States.

Author Contributions

△A.G.B. and A.A.A. contributed equally to this work.

Notes

The authors declare no competing financial interest.

■ ACKNOWLEDGMENTS

We would like to thank Dr. Michael Ross and the Peidong Yang lab at University of California, Berkeley, Department of Chemistry for help with Raman measurements. We acknowledge startup funding from the University of Texas at El Paso (to A.A.A. and L.V.), the NSF Division of Materials Research, Grant No. 1506886 (to P.K.), Burroughs Wellcome Fund Career Award at the Scientific Interface (CASI) (M.P.L.), the Simons Foundation (M.P.L.), a Stanley Fahn PDF Junior Faculty Grant with Award No. PF-JFA-1760 (M.P.L.), a Beckman Foundation Young Investigator Award (M.P.L.), and a DARPA Young Investigator Award (M.P.L.). M.P.L. is a Chan Zuckerberg Biohub investigator. A.G.B. is supported by an NSF Graduate Research Fellowship and an NIH F99/K00 award from NINDS. The authors gratefully acknowledge computer time provided by the Texas Advanced Computing Center (TACC). This research is part of the Blue Waters sustained-petascale computing project, which is supported by the National Science Foundation (Award Nos. OCI-0725070 and ACI-1238993) and the state of Illinois.

■ REFERENCES

(1) Kang, S. J.; et al. High-performance electronics using dense, perfectly aligned arrays of single-walled carbon nanotubes. *Nat. Nanotechnol.* **2007**, *2*, 230.
(2) McEuen, P. L.; Fuhrer, M. S.; Park, H. Single-walled carbon nanotube electronics. *IEEE Trans. Nanotechnol.* **2002**, *1*, 78.
(3) Baughman, R. H.; Zakhidov, A. A.; De Heer, W. A. Carbon nanotubes - The route toward applications. *Science* **2002**, *297*, 787.
(4) LeMieux, M. C.; et al. Self-sorted, aligned nanotube networks for thin-film transistors. *Science (Washington, DC, U. S.)* **2008**, *321*, 101.
(5) He, X.; et al. Tunable room-Temperature single-photon emission at telecom wavelengths from sp 3 defects in carbon nanotubes. *Nat. Photonics* **2017**, *11*, 577.
(6) Barone, P. W.; Baik, S.; Heller, D. A.; Strano, M. S. Near-infrared optical sensors based on single-walled carbon nanotubes. *Nat. Mater.* **2004**, *4*, 86.
(7) Satishkumar, B. C.; et al. Reversible fluorescence quenching in carbon nanotubes for biomolecular sensing. *Nat. Nanotechnol.* **2007**, *2*, 560.
(8) Oliveira, S. F.; et al. Protein functionalized carbon nanomaterials for biomedical applications. *Carbon* **2015**, *95*, 767.
(9) Zhang, J.; et al. Molecular recognition using corona phase complexes made of synthetic polymers adsorbed on carbon nanotubes. *Nat. Nanotechnol.* **2013**, *8*, 959.
(10) Pu, K. et al. Supporting Information for Semiconducting polymer nanoparticles as photoacoustic molecular imaging probes in living mice. *Nat. Nanotechnol.* 2014. DOI: 10.1038/nnano.2013.302\r. http://www.nature.com/nnano/journal/v9/n3/abs/nnano.2013.302.html#supplementary-information.
(11) Bonis-O'Donnell, J. T. D.; et al. Dual Near-Infrared Two-Photon Microscopy for Deep-Tissue Dopamine Nanosensor Imaging. *Adv. Funct. Mater.* **2017**, *27*, 1702112.
(12) Hong, G.; et al. Through-skull fluorescence imaging of the brain in a new near-infrared window. *Nat. Photonics* **2014**, *8*, 723.
(13) Godin, A. G.; et al. Single-nanotube tracking reveals the nanoscale organization of the extracellular space in the live brain. *Nat. Nanotechnol.* **2017**, *12*, 238.
(14) Král, P.; Wang, B. Material drag phenomena in nanotubes. *Chem. Rev.* **2013**, *113*, 3372.
(15) Geng, J.; et al. Stochastic transport through carbon nanotubes in lipid bilayers and live cell membranes. *Nature* **2014**, *514*, 612.
(16) Holt, J. K. Fast mass transport through sub-2-nanometer carbon nanotubes. *Science (Washington, DC, U. S.)* **2006**, *312*, 1034.

DOI: 10.1021/acs.nanolett.8b02937
Nano Lett. 2018, 18, 6995−7003

(17) Cognet, L.; et al. Stepwise quenching of exciton fluorescence in carbon nanotubes by single-molecule reactions. *Science (Washington, DC, U. S.)* **2007**, *316*, 1465.
(18) Dukovic, G.; et al. Reversible surface oxidation and efficient luminescence quenching in semiconductor single-wall carbon nanotubes. *J. Am. Chem. Soc.* **2004**, *126*, 15269.
(19) Lee, A. J.; et al. Bright fluorescence from individual single-walled carbon nanotubes. *Nano Lett.* **2011**, *11*, 1636.
(20) Kim, J. H.; et al. The rational design of nitric oxide selectivity in single-walled carbon nanotube near-infrared fluorescence sensors for biological detection. *Nat. Chem.* **2009**, *1*, 473.
(21) Kruss, S.; et al. Neurotransmitter detection using corona phase molecular recognition on fluorescent single-walled carbon nanotube sensors. *J. Am. Chem. Soc.* **2014**, *136*, 713.
(22) Giraldo, J. P.; et al. A Ratiometric Sensor Using Single Chirality Near-Infrared Fluorescent Carbon Nanotubes: Application to In Vivo Monitoring. *Small* **2015**, *11*, 3973.
(23) Bisker, G.; et al. Protein-targeted corona phase molecular recognition. *Nat. Commun.* **2016**, *7*, 10241.
(24) Harvey, J. D.; et al. A carbon nanotube reporter of microRNA hybridization events in vivo. *Nat. Biomed. Eng.* **2017**, *1*, 0041.
(25) Heller, D. A.; et al. Multimodal optical sensing and analyte specificity using single-walled carbon nanotubes. *Nat. Nanotechnol.* **2009**, *4*, 114.
(26) Sun, H.; Ren, J.; Qu, X. Carbon Nanomaterials and DNA: From Molecular Recognition to Applications. *Acc. Chem. Res.* **2016**, *49*, 461.
(27) Alivisatos, A. P.; et al. Nanotools for neuroscience and brain activity mapping. *ACS Nano* **2013**, *7*, 1850.
(28) Beyene, A. G.; McFarlane, I. R.; Pinals, R. L.; Landry, M. P. Stochastic Simulation of Dopamine Neuromodulation for Implementation of Fluorescent Neurochemical Probes in the Striatal Extracellular Space. *ACS Chem. Neurosci.* **2017**, *8*, 2275.
(29) Dreyer, J. K.; Herrik, K. F.; Berg, R. W.; Hounsgaard, J. D. Influence of Phasic and Tonic Dopamine Release on Receptor Activation. *J. Neurosci.* **2010**, *30*, 14273.
(30) Beyene, A. G.; Demirer, G. S.; Landry, M. P. Nanoparticle-Templated Molecular Recognition Platforms for Detection of Biological Analytes. *Curr. Protoc. Chem. Biol.* **2016**, 197.
(31) Park, J.; Takmakov, P.; Wightman, R. M. In vivo comparison of norepinephrine and dopamine release in rat brain by simultaneous measurements with fast-scan cyclic voltammetry. *J. Neurochem.* **2011**, *119*, 932.
(32) Sulzer, D.; Cragg, S. J.; Rice, M. E. Striatal dopamine neurotransmission: Regulation of release and uptake. *Basal Ganglia* **2016**, *6*, 123.
(33) Landry, M. P.; et al. Comparative Dynamics and Sequence Dependence of DNA and RNA Binding to Single Walled Carbon Nanotubes. *J. Phys. Chem. C* **2015**, *119*, 10048.
(34) Heller, D. a.; et al. Optical detection of DNA conformational polymorphism on single-walled carbon nanotubes. *Science* **2006**, *311*, 508.
(35) Salem, D. P.; et al. Ionic Strength-Mediated Phase Transitions of Surface-Adsorbed DNA on Single-Walled Carbon Nanotubes. *J. Am. Chem. Soc.* **2017**, *139*, 16791.
(36) Bergler, F. F.; Schöppler, F.; Brunecker, F. K.; Hailman, M.; Hertel, T. Fluorescence spectroscopy of gel-immobilized single-wall carbon nanotubes with microfluidic control of the surfactant environment. *J. Phys. Chem. C* **2013**, *117*, 13318.
(37) Jena, P. V.; Safaee, M. M.; Heller, D. A.; Roxbury, D. DNA-Carbon Nanotube Complexation Affinity and Photoluminescence Modulation Are Independent. *ACS Appl. Mater. Interfaces* **2017**, *9*, 21397.
(38) Schöppler, F.; et al. Molar Extinction Coefficient of Single-Wall Carbon Nanotubes. *J. Phys. Chem. C* **2011**, *115*, 14682.
(39) Gigliotti, B.; Sakizzie, B.; Bethune, D. S.; Shelby, R. M.; Cha, J. N. Sequence-independent helical wrapping of single-walled carbon nanotubes by long genomic DNA. *Nano Lett.* **2006**, *6*, 159.
(40) Johnson, R. R.; Johnson, a T. C.; Klein, M. L. Probing the Structure of DNA− Carbon Nanotube Hybrids with Molecular Dynamics. *Nano Lett.* **2008**, *8*, 69.
(41) Dukovic, G.; et al. Racemic single-walled carbon nanotubes exhibit circular dichroism when wrapped with DNA. *J. Am. Chem. Soc.* **2006**, *128*, 9004.
(42) Johnson, R. R.; Kohlmeyer, A.; Johnson, a T. C.; Klein, M. L. Free energy landscape of a DNA-carbon nanotube hybrid using replica exchange molecular dynamics. *Nano Lett.* **2009**, *9*, 537.
(43) Manohar, S.; Tang, T.; Jagota, A. Structure of homopolymer DNA-CNT hybrids. *J. Phys. Chem. C* **2007**, *111*, 17835.
(44) Patra, N.; Song, Y.; Král, P. Self-assembly of graphene nanostructures on nanotubes. *ACS Nano* **2011**, *5*, 1798.
(45) Jena, P. V.; et al. A Carbon Nanotube Optical Reporter Maps Endolysosomal Lipid Flux. *ACS Nano* **2017**, *11*, 10689.
(46) Perebeinos, V.; Avouris, P. Phonon and electronic nonradiative decay mechanisms of excitons in carbon nanotubes. *Phys. Rev. Lett.* **2008**, *101*, 057401.
(47) Sau, J. D.; Crochet, J. J.; Doorn, S. K.; Cohen, M. L. Multiparticle exciton ionization in shallow doped carbon nanotubes. *J. Phys. Chem. Lett.* **2013**, *4*, 982.
(48) Ivchenko, E. L.; et al. Exciton logitudinal-transverse splitting in GaAs/AlGaAs superlattices and multiple quantum wells. *Solid State Commun.* **1989**, *70*, 529.

NOTE ADDED AFTER ASAP PUBLICATION

This paper published ASAP on 10/25/2018 with an incomplete TOC/Abstract image. It was corrected and the revised version was reposted on 10/26/2018. A correction to the Supporting Information was missing from the original ASAP posting. The revised version was reposted on 10/31/2018.

DOI: 10.1021/acs.nanolett.8b02937
Nano Lett. 2018, 18, 6995−7003